IEEE Robotics and Automation Letters (RAL) paper presented at the
2020 IEEE/RSJ International Conference on Intelligent Robots and Systems (IROS)
October 25-29, 2020, Las Vegas, NV, USA (Virtual)

A Realistic Simulation Environment for MRI-based Robust Control of Untethered Magnetic Robots with Intra-Operational Imaging

Mehmet Efe Tiryaki[1], Önder Erin[1,2], Metin Sitti[1,2,3]

***Abstract*— Dual-use of magnetic resonance imaging (MRI) devices for robot tracking and actuation has transformed them into potential medical robotics platforms for targeted therapies and minimally invasive surgeries. In this paper, we present the dynamic simulations of an MRI-based tracking and actuation scheme, which performs intra-operational imaging while controlling untethered magnetic robots. In our realistic rigid-body simulation, we show that the robot could be controlled with a 1D projection-based position feedback while performing intra-operational echo-planar imaging (EPI). From the simulations, we observe that the velocity estimation error is the main source of the controller instability for low MRI sequence frequencies. To minimize the velocity estimation errors, we constrain the controller gains according to maximum closed-loop rates achievable for different sequence durations. Using the constrained controller in simulations, we confirm that EPI imaging could be introduced to the sequence as an intra-operational imaging method. Although the intro-operational imaging increases the position estimation error to 2.0 mm for a simulated MRI-based position sensing with a 0.6 mm Gaussian noise, it does not cause controller instability up to 128 k-space lines. With the presented approach, continuous physiological images could be acquired during medical operations while a magnetic robot is actuated and tracked inside an MRI device.**

I. Introduction

Performing medical operations, such as targeted therapies and minimally invasive surgeries, with robots require medical systems that are capable of localizing and manipulating the robot while being able to visualize the anatomical structure of the patient's body [1], [2]. The MRI scanners have been proposed as a promising medical imaging platform that can localize and actuate magnetic robots using specialized tracking and actuation sequences [3]–[7]. While some of these sequences are capable of performing high-bandwidth tracking and actuation [4]–[6] without imaging, others are capable of imaging without high-bandwidth tracking and actuation [7], [8]. Minimally invasive medical operations inside MRI scanners, such as targeted drug delivery and local hyperthermia, in hard-to-access and high health-risk areas of the human body, requires both high-bandwidth position feedback for robot control and continuous image of the surrounding tissue for precise and safe operation. [2].

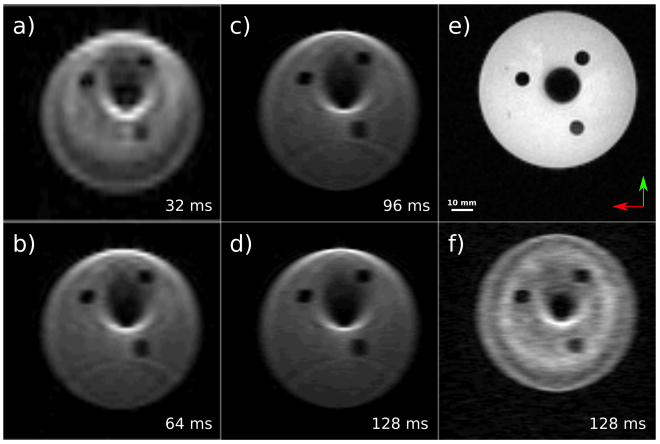

Fig. 1: Experimental MRI images of a circular phantom filled with agarose gel with a 250 µm-radius chrome steel bead at the center and three Plexiglas reference markers around it. The volumetric saturation magnetization of the steel bead is measured as 9.19×10^5 A/m using vibrating sample magnetometer (EZ7, MicroSense, Massachusetts, USA). Red and green axes of images are frequency and phase encoding direction, respectively. The samples are imaged by a 7-Tesla MRI BioSpec 70/30 (Bruker, Ettlingen, Germany). All images have 3 mm slice thickness, 102×102 field of view, and 96 resolution in frequency encoding direction, and they are oriented in the axial plan. a-d) Images are taken by single-shot Cartesian spin-echo EPI with k-space line number in alphabetic order $\{32, 64, 96, 128\}$ in phase encoding directions, 90° flip angle TE = 20.12 ms, and TR given on the images. e) Image is taken by FLASH with flip angle 15°, TE/TR = 1.79/5.0 ms, and total acquisition duration: 480 ms. f) Experimental image is taken by multi-shot EPI with 4 segmentation with 128 k-space line in phase encoding direction, 90° flip angle TE = 20.12 ms, TR = 32 ms per segment, and total acquisition duration: 128 ms.

In order to combine the advantages of two approaches, we present an MRI sequence with intra-operational echo-planar imaging (EPI) for magnetic robot control. A control scheme composing of a linear Kalman filter estimating robot position and velocity, and a proportional-derivative (PD) controller are implemented for a broad range of MRI sequence parameters for buoyant operating conditions in the water. We study the effect of the MRI sequence parameters on state estimation and controller performance using dynamic robot simulations. For the first time, we simulate the MRI actuation and position feedback mechanism with realistic timings and gradients. In the simulation, the robot position is assumed to be obtained by a 1D projection-based tracking method. We investigate the closed-loop system rate through state-space representation. We demonstrated the effect of the actuation duration on state estimation and controller performance without intra-operational imaging. Then, we quantify

Manuscript received: February 21, 2020; Revised May 18, 2020; Accepted June, 02 , 2020.
This paper was recommended for publication by Editor Pietro Valdastri upon evaluation of the Associate Editor and Reviewers' comments. This work is funded by the Max Planck Society
[1] Physical Intelligence Department, Max Planck Institute for Intelligent Systems, Stuttgart 70569, Germany. E-mail: sitti@is.mpg.de
[2] Mechanical Engineering Department, Carnegie Mellon University, Pittsburgh, PA 15213, USA.
[3] School of Engineering and School of Medicine, Koç University, Istanbul 34450, Turkey.
Digital Object Identifier (DOI): see top of this page.

the trajectory-following performance of the controller with different durations of intra-operational imaging introduced into the tracking and actuation sequence. We also report example EPI images of a ferromagnetic bead in an agarose gel phantom in Fig. 1, which are acquired with different EPI sequence durations.

II. Related Work

The majority of MRI tracking and actuation sequences use magnetic gradient forces to actuate untethered magnetic robots. However, they have different tracking methods [5]–[7]. There are two main techniques to localize magnetic robots under MRI. The first technique is localization by performing a special 1D-projection imaging method called magnetic signature selective excitation tracking (MS-SET) [4]. The selective excitation of the region around the magnetic robot enables MS-SET to obtain position information for each axis within a relatively short duration, such as ∼5.5 ms [6]. Such tracking speed results in a 60 Hz sampling frequency for 3D position feedback in the absence of actuation. Tamaz et al. [5] demonstrated control of a ferromagnetic bead using MS-SET and 15 ms actuation duration, resulting in an alternating tracking and actuation sequence at 33 Hz bandwidth. Later in [6], Felfoul et al. proposed an approach for steering ferromagnetic beads in constrained channels by performing MS-SET only in the direction of the desired actuation. This simultaneous tracking and actuation method boosts overall actuation frequency up to 180 Hz. Moreover, they also reported that the average magnetic actuation force could be much higher than the alternating tracking and actuation approach. However, the simultaneous tracking and actuation method is limited to motion in channel-like structures and there is no controller scheme proposed for more general operating conditions. While MS-SET has the potential to provide the 3D position of a magnetic robot in the patient's body, it cannot provide any anatomical detail of the body. Therefore, tracking and actuation sequences using MS-SET should be accompanied by an inter-operational imaging of anatomical structures. In other words, the alternating tracking and actuation sequence should be interrupted during operation to perform traditional MR physiological imaging, which leaves the robot uncontrolled during such imaging.

The second technique for magnetic robot localization is MR image-based visual-servoing approach, which uses intra-operational imaging while actuating the magnetic robots [7], [8]. The main handicap of these proof-of-concept studies are the long imaging duration of 960 ms [8], which also leaves the robots virtually uncontrolled during such imaging, as in the inter-operational imaging case. Such an extended imaging and actuation scheme is prohibitively slow for MRI-based visual-servoing of magnetic robots. As an alternative, MRI literature offers rich options for ultra-fast imaging sequences, such as single-shot radio frequency (RF) excitation EPI sequences [9], which could be used in tracking and actuation sequences. Furthermore, using parallel imaging techniques [10], [11] and MR image acceleration algorithms [12]–[15] reconstructing images with under-sampled k-space data, the time allocated for intra-operational imaging can be further decreased.

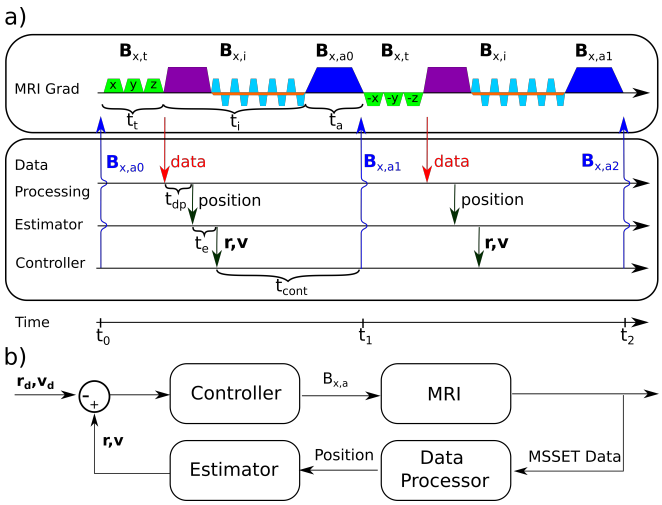

Fig. 2: a) Top block shows two tracking and actuation sequence repetitions with single-shot EPI as the intra-operational imaging method. The tracking gradients are shown with three green blocks representing three orthogonal projection directions. The direction is reversed in each repetition. The dark purple pulse represents the average of slice selection and refocusing gradients of single-shot spin echo EPI sequence. Light blue and orange pulses represent frequency encoding and phase encoding of zigzag k-space trajectories, respectively. The dark blue is the actuation gradient. Bottom block shows software structure for the robot controller scheme. Blue arrows are the actuation magnetic fields calculated by the controller. Red arrow is the MRI signal for robot position tracking. t_{t}, t_{i}, t_{a}, t_{dp}, t_{e}, and t_{cont} are the durations for tracking, imaging, actuation, data processing, estimation, and control, respectively. b) Block-diagram of the overall control scheme.

Besides the MRI sequence design, in order to evaluate the overall performance of the MRI-based control schemes, the simulation becomes an indispensable tool due to the low accessibility of MRI scanners. While there are a few simulation studies, which captures different physical phenomena, such as hydrodynamics and electrostatic forces on MRI-based robots [16]–[21], these simulation works do not address some of the most important aspects of MRI-based actuation and feedback mechanisms. Arcese et al. [17], [18] include MRI's maximum magnetic gradient limitations in their simulations. Belharet [19] and Eqtami [20] include the sampling time of MRI-based feedback as 100 ms and 20 ms, respectively. In addition to the sampling rate, [20] also mentions the delays due to the computation. Lastly, in our previous work [22], we presented a Gazebo-based dynamic robotic simulation that applies the actuation gradient considering MRI sequence timing. However, this previous work does not consider MRI-based tracking and imaging gradients and does not realistically simulate MRI-based position feedback. Therefore, to the best of our knowledge, there is no realistic simulation environment in literature fully capturing the MRI-based feedback and actuation.

III. System Description

MRI devices operate through predefined pulse sequences. Therefore, to control the magnetic robots, we present a

tracking and actuation sequence with intra-operational imaging (Fig. 2). The MRI runs the sequence repeatedly while communicating with an external controller software. In each sequence repetition, the position information obtained from the MRI system using MS-SET is fed to the state estimator after a short data processing duration shown as t_{dp} in Fig. 2. The state estimator passes the estimated robot state composed of position and velocity to the controller. The calculated control input is then sent to the MRI to be applied in the upcoming sequence. The MRI sequence programming systems do not allow any change in gradient values once a sequence repetition starts. Therefore, if the total duration for control signal calculation $\bar{t}_{\text{cont}} = t_{\text{dp}} + t_{\text{e}} + t_{\text{cont}}$ is greater than $t_{\text{i}} + t_{\text{a}}$, the control signal can only be applied in next sequence repetition.

A. Magnetic Gradient-based Robot Actuation

Assuming a uniform magnetization, the magnetic pulling force acting on a ferromagnetic bead in the MRI scanner is calculated as

$$\mathbf{F}_m = V_{\text{m}}(\mathbf{M} \cdot \nabla)\mathbf{B}. \tag{1}$$

Here, V_{m} is the magnetic volume of the robot, which can be written as $V_{\text{m}} = \gamma V$, where γ is the magnetic volume ratio and V is the volume of the robot. $\mathbf{M} \in \mathbb{R}^3$ is the volumetric magnetization vector of ferromagnetic core, and $\mathbf{B} \in \mathbb{R}^3$ is the magnetic field acting on the robot. Since the main magnetic field of the MRI scanner[1], $\mathbf{B}_0 = B_0\hat{\mathbf{x}}$, where $\hat{\mathbf{x}}$ is the unit vector in x axis, is much larger than the magnetic field generated by gradient coils, the magnetization of the ferromagnetic core is always oriented in the direction of $\mathbf{B}_0$ [21]. Hence, (1) can be written as

$$\mathbf{F}_m = V_{\text{m}} M \mathbf{B}_x, \tag{2}$$

where M is the scalar volumetric magnetization in the axial direction, and $\mathbf{B}_x = \nabla(\hat{\mathbf{x}} \cdot \mathbf{B})$ with ∇ being the gradient operator [3].

In a tracking and actuation sequence, the average magnetic gradient of the sequence is also important, and it is defined as

$$\bar{\mathbf{B}}_x = \beta_a \mathbf{B}_{x,a} + \beta_i \mathbf{B}_{x,i} + (1 - \beta_a - \beta_i)\mathbf{B}_{x,t}. \tag{3}$$

β_a and β_i are the ratio of actuation and imaging to the sequence length, and $\mathbf{B}_{x,a}$, $\mathbf{B}_{x,i}$, and $\mathbf{B}_{x,t}$ are actuation, imaging and tracking gradients, respectively. Since we can cancel the effect of the tracking gradients by reversing the readout direction of the tracking projections in each sequence repetition, as shown in Fig. 2 [4]. The resultant average magnetic field for two sequence repetition can be written as

$$\tilde{\mathbf{B}}_x = \beta_a \mathbf{B}_{x,a} + \beta_i \mathbf{B}_{x,i}. \tag{4}$$

[1]In this paper, the axial direction (main field direction) of the MRI scanner is chosen as x axis, and upward direction is chosen as z axis.

This equation can be further simplified if imaging sequences are used symmetrically. However, in a typical operation scenario, the imaging gradients might change depending on the chosen image slice position and orientation; therefore, we keep this term.

B. Robot Design

We use a symmetric spherical ferromagnetic chrome steel bead as our magnetic robot to simplify the models. The available magnetic force in the MRI scanner is not enough to compensate for the weight of the robot in the water, and such weight compensation would limit the controller performance by constraining the controller gains. Therefore, we assumed that the robot is covered with a light density spherical shell resulting in a near buoyant design similar to [21] for a 750 µm-radius robot. The density of the overall robot is calculated as

$$\rho = \gamma \rho_m + (1 - \gamma)\rho_s \tag{5}$$

where ρ_m and ρ_s are the density of the ferromagnetic core and the density of the shell, respectively. In the ideal case, the density of the robot should be equal to the density of the fluid at operating temperatures, $\rho_f(T)$. Therefore, we can calculate the required shell density with respect to the magnetic volume as

$$\rho_s = \frac{\rho_f(T) - \gamma \rho_m}{1 - \gamma}. \tag{6}$$

From (6), we can see that γ should be strictly smaller than $\rho_f(T)/\rho_m$ and the average density of the shell depends on the magnetic volume ratio. On the other hand, decreasing the magnetic volume ratio also decreases the available magnetic force for control purposes.

C. Hydrodynamic Forces

There are two major hydrodynamic forces acting on the robot. First one is buoyancy force,

$$\mathbf{F}_{\text{b}} = V \rho_f(T) g \hat{\mathbf{z}}, \tag{7}$$

where g is the gravitational acceleration constant and $\hat{\mathbf{z}}$ is the unit vector in z axis. In case of a density mismatch between robot density and fluid density, $\delta\rho = \rho_f(T) - \rho$, the apparent weight of the robot is calculated as

$$\mathbf{F}_{\text{w}} = V \delta\rho g \hat{\mathbf{z}}. \tag{8}$$

The second hydrodynamic forces acting on the robot is the hydrodynamic drag forces. We calculated the drag forces acting on the robot as

$$\mathbf{F}_d = -\frac{1}{2} C_{\text{d}} \rho_f A \left|\mathbf{v}_{\text{f}} - \mathbf{v}\right|^2 \frac{\mathbf{v}_{\text{f}} - \mathbf{v}}{\left|\mathbf{v}_{\text{f}} - \mathbf{v}\right|}, \tag{9}$$

where A is the cross-sectional area of the robot, and $\mathbf{v} \in \mathbb{R}^3$ and $\mathbf{v}_{\text{f}} \in \mathbb{R}^3$ are the velocity of the robot and fluid in the inertial frame, respectively. Since our robot operates in Reynold's number $Re = 2r\rho_{\text{f}}\left|\mathbf{v}_{\text{f}} - \mathbf{v}\right|/\mu < 10$, where r is

the radius of the robot, μ is the dynamic viscosity of the fluid, the drag coefficient C_d is calculated using laminar flow assumption [23] as:

$$C_\mathrm{d} = \frac{24}{Re} + \frac{6}{1+\sqrt{Re}} + 0.4. \tag{10}$$

D. State Estimation

The MRI-based tracking sequence only provides the 3D position of the robot; therefore, in order to use velocity-based controllers, the unmeasured robot velocity should be estimated from the position data as in [17]. We used linear Kalman filter to estimate the robot position and velocity for 3D motion using Stoke's drag formula [1] $F_\mathrm{st} = 6\pi\mu r|\mathbf{v}_\mathrm{f} - \mathbf{v}|$. While the discrepancy between (9) and Stoke's drag is small for low velocities, the difference in drag forces reaches 35% of laminar flow drag for the limit of our operation limits.

Since the assumed process model is linear, we can treat each axis independent, and 1D dynamics of the system can be as

$$\mathbf{x}_{\mathrm{k}+1} = \underbrace{\begin{bmatrix} 1 & \Delta t \\ 0 & 1-\alpha\Delta t \end{bmatrix}}_{\Phi} \mathbf{x}_\mathrm{k} + \underbrace{\frac{1}{m}\begin{bmatrix} \Delta t^2/2 \\ \Delta t \end{bmatrix}}_{\Gamma} (u_\mathrm{k} + w_k) \tag{11}$$

where the state, $\mathbf{x}_\mathrm{k} \in \mathbb{R}^2$, is composed of position and velocity of the robot. $u_k \in \mathbb{R}$ is the acceleration due to the magnetic force and the apparent weight, and w_k is the process noise in terms of uncorrelated acceleration noise with zero mean. The linear deceleration due to the linear fluid drag is $\alpha = 6\pi\mu r/m$. Δt is the total duration of an MRI sequence repetition. The measurement for each dimension is

$$\mathbf{z}_\mathrm{k} = \underbrace{\begin{bmatrix} 1 & 0 \end{bmatrix}}_{\mathbf{H}} \mathbf{x}_\mathrm{k} + v_k, \tag{12}$$

where v_k is the measurement noise with zero mean. It is assumed that the measurement is done at the end of the tracking gradient. Then the standard Kalman filter formulation is used for each direction [24]. The prediction step is

$$\hat{\mathbf{x}}_{\mathrm{p,k}+1} = \Phi\hat{\mathbf{x}}_{\mathrm{m,k}} + \Gamma u_\mathrm{k} \tag{13}$$

$$\mathbf{P}_{\mathrm{p,k}+1} = \Phi\mathbf{P}_{\mathrm{m,k}}\Phi^\mathrm{T} + \Gamma\mathbf{Q}\Gamma^\mathrm{T} \tag{14}$$

and the measurement step is

$$\hat{\mathbf{x}}_{\mathrm{m,k}+1} = \hat{\mathbf{x}}_{\mathrm{p,k}+1} + \mathbf{K}(\mathbf{z}_{\mathrm{k}+1} - \mathbf{H}\hat{\mathbf{x}}_{\mathrm{p,k}+1}) \tag{15}$$

$$\mathbf{P}_{\mathrm{m,k}+1} = (\mathbb{I} - \mathbf{K}_{\mathrm{k}+1}\mathbf{H})\mathbf{P}_{\mathrm{p,k}+1} \tag{16}$$

where $\hat{\mathbf{x}}_{\mathrm{p,k}} \in \mathbb{R}^2$ and $\hat{\mathbf{x}}_{\mathrm{m,k}} \in \mathbb{R}^2$ are the predicted state and measurement updated state at time step k, respectively. The Kalman gain is $\mathbf{K}_{\mathrm{k}+1} = \mathbf{P}_{\mathrm{p,k}+1}\mathbf{H}^\mathrm{T}(\mathbf{H}\mathbf{P}_{\mathrm{p,k}+1}\mathbf{H}^\mathrm{T} + \mathbf{R})^{-1}$ and $\mathbb{I}$ is 2×2 identity matrix. While calculating the prediction step, we used the sequence average magnetic gradient. The accuracy of the prediction can be increased by performing the estimation with finer time-steps capturing the individual effect of each gradient in the sequence. However, because of the short time window for the state estimator and controller before the next sequence starts, we avoid computationally expensive prediction at the cost of lower accuracy.

E. Controller

Although different controllers were proposed for MRI-based actuation [16]–[19], [25], we have used an acceleration reference-based PD controller with apparent weight and imaging gradient compensation to simplify our analysis. We define the control law for the actuation gradient as

$$\mathbf{B}_{x,a} = \frac{1}{\beta_a}\left(\frac{1}{V_\mathrm{m}M}(m\mathbf{a}_{ref} - \mathbf{F}_w) - \beta_i\mathbf{B}_{x,i}\right), \tag{17}$$

where

$$\mathbf{a}_{ref} = \mathbf{K}_\mathrm{p}(\mathbf{r}_d - \mathbf{r}) + \mathbf{K}_\mathrm{d}(\mathbf{v}_d - \mathbf{v}). \tag{18}$$

$\mathbf{K}_\mathrm{p} = k_\mathrm{p}\mathrm{diag}(1,1,1)$ and $\mathbf{K}_\mathrm{d} = k_\mathrm{d}\mathrm{diag}(1,1,1)$ are the diagonal proportional and derivative gain matrices, respectively. $\mathbf{r} \in \mathbb{R}^3$ is the robot position. $\mathbf{r}_d \in \mathbb{R}^3$ and $\mathbf{v}_d \in \mathbb{R}^3$ are desired position and velocity, respectively. Formulating the control law in this way, we can use the same controller parameters for sequence with different actuation and intra-operation imaging durations. In practice, an integrator term can also be added to the acceleration reference in order to eliminate small discrepancies in the model. Since our controller has almost complete knowledge of the system, we do not use the integrator term to facilitate the following analysis.

Sequences with different durations have different capacities to handle the closed-loop dynamics. In order to perform a fair comparison among sequences with various durations, we identify approximate closed-loop rates of the controller or a sequence using a linear drag assumption. Using (17), we can write the continuous closed-loop dynamics of each direction in the following form

$$\dot{\mathbf{x}} = \begin{bmatrix} 0 & 1 \\ 0 & -\alpha \end{bmatrix}\mathbf{x} + \begin{bmatrix} 0 \\ 1 \end{bmatrix}\mathbf{a}_{ref} \tag{19}$$

where $\mathbf{x} \in \mathbb{R}^2$ is the state composed of position and velocity in one direction. By substituting (18) into (19), the eigenvalues of the continuous dynamics for each direction can be calculated in terms of k_p and k_d, which are diagonal elements of gain matrices, as

$$\lambda = -\frac{\alpha + k_\mathrm{d}}{2}\left(1 \pm \sqrt{1 - \frac{4k_\mathrm{p}}{(\alpha+k_\mathrm{d})^2}}\right). \tag{20}$$

λ is a complex variable expressing damping and oscillations rates of the continuous dynamics. We use (20) to obtain a general relation between k_p and k_d and the maximum allowable closed-loop rates, $\bar{\lambda}$, for different MRI sequence frequencies, $f_\mathrm{seq} = 1/(t_t + t_i + t_a)$. We define following rate constraint based on MRI sequence frequency:

$$f_{seq}/\mathscr{N} = \bar{\lambda} > |\lambda| \tag{21}$$

where $\mathscr{N} \in \mathbb{R}_{>0}$ defines the upper limit of the targeted closed-loop rate, $\bar{\lambda}$, with respect to the MRI sequence frequency, f_seq. The higher $\bar{\lambda}$ is, the faster the controller react to errors. However, we are constrained by f_seq due to

the limited position feedback rate. Using (20) and (21), after considerable algebraic manipulations, we obtain maximum $\bar{k}_p$ value as a function of k_d and targeted maximum closed-loop rate,

$$\bar{k}_\mathrm{p}(k_\mathrm{d},\bar{\lambda}) = \bar{\lambda}^2 - \bar{\lambda}(\alpha + k_\mathrm{d}) + (\alpha + k_\mathrm{d})^2/2. \qquad (22)$$

k_d values in $[0, 2\bar{\lambda} - \alpha]$ satisfy the stability criteria [26] and also (21). Depending on the desired damping ratio $\zeta = (\alpha + k_\mathrm{d})/(2\sqrt{k_\mathrm{p}})$ and $\mathcal{N}$, we can choose k_p and k_d values for different sequence frequencies.

F. Intra-operational Imaging

In addition to the robot tracking with MS-SET and actuation with magnetic gradients, the third and arguably the most important functionality of the MRI is to obtain intra-operational images of the physiological operation environment during the robot actuation. MR imaging literature offers vast options for fast imaging techniques. For instance, Dahmen et al. [7] use half-Fourier acquisition single-shot turbo spin-echo and fast low angle shot (FLASH). These are examples of multiple excitation spin-echo and gradient-echo imaging techniques, which acquires the k-space data of the image line by line. In order to obtain high-resolution images, these sequences excite the spins of the specimen before each k-space line acquisition and contain long repetition duration to separate signal received from different k-space lines.

Even with these high-resolution imaging techniques, imaging a magnetic robot is still challenging. By altering the Larmor frequency of the nearby protons, the magnetic robot creates an image artifact obscuring a significant part of the image. An example of an experimental FLASH image is given in Fig. 1e. It can be seen that 250 µm-radius chrome steel has created an imaging artifact approximately 20 times of the robot's size. Similar imaging artifacts are also reported in [21], [27], [28]. Although there are techniques [29], [30] proposed for reducing metal artifacts, these techniques increase total imaging duration. Since we have limited time for imaging, the high-resolution and low distortion images are expensive in terms of time for control purposes.

On the other hand, the EPI sequence offers a relatively short imaging duration at the cost of image quality. EPI sequences are so-called ultrafast imaging sequences, which applies single-shot RF excitation to collect multiple k-space lines at once with a zigzag k-space trajectory coverage, rather than applying RF excitation for each k-space line. Example experimental EPI images of the ferromagnetic bead with different resolutions are given in Fig. 1a-d. Although the magnetic susceptibility creates a significantly larger artifact in Fig. 1a-d, since EPI is superior to other techniques in respect of speed, we use the k-space line acquisition time of EPI as a reference in this study.

Properties	**Values**
Robot radius (µm)	750
Robot density (g/cm^3)	1.0
Magnetic volume ratio	0.064
Magnetization (A/m)	9.2e5
Temperature (°C)	36
Fluid density (g/cm^3)	0.993
Fluid viscosity (Pa·s)	7e-4
Fluid flow (mm/s)	0.0
Tracking duration (ms)	16.5
Average tracking gradient (mT/m)	0.453
Maximum allowable actuation gradient (mT/m)	66
Position sensor noise standard deviation (mm)	0.6
Simulation time step (ms)	1
Kalman filter **Q**	1.0e-11diag(1,1,1)
Kalman filter **R**	1.0e-3 diag(1,1,1)

TABLE I: Simulation parameters

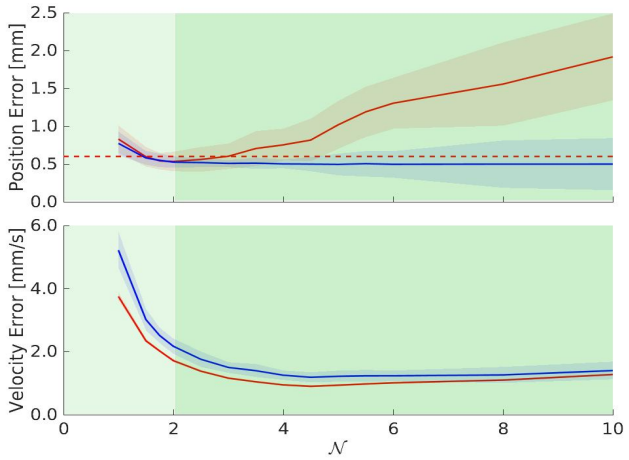

Fig. 3: The simulation plots demonstrate average mean-square position and velocity error of trajectory following (red) and estimation (blue) for 40 experiments for each $\mathcal{N}$. The transparent region around data represents the standart devitaion. The light green area shows the cases when closed-loop rate of the system is above Nyquist's rate. Higher $\mathcal{N}$ corresponds to lower control gains and vice versa.

IV. Simulation Results

In this study, we use the Gazebo [31] simulation environment to evaluate the effect of the MRI sequence to the controller and the estimator performance. In addition to the existing rigid-body dynamic framework of Gazebo, we implement our own fluid and magnetic force modules. The fluid module contains the drag force calculated by (9) and buoyancy force (7) of the fluid. We used temperature-depended empirical density and viscosity of the water [32], [33].

The magnetic forces due to the MRI sequence is calculated using (2). The magnetic gradients are assumed uniform in the workspace with a maximum available amplitude of 66 mT/m due to the MRI hardware limitations, and the rise time of the gradient pulses are neglected. To capture the effect of gradient pulses, which are shorter than the simulation time step, we average all the magnetic forces lying within each time step. For the realistic simulation of MRI actuation and tracking conditions, the received actuation signal is applied in upcoming sequence repetition, and the position data for each axis is collected at the beginning of the corresponding axis' tracking gradient pulse. Then the collected data is published to state estimator after a simulated computation and communication duration. Although Felfoul et al. [6]

report this duration as 10 ms, we use our Biospec 70/30 MRI (Bruker, Etlingen, Germany) scanner's Paravision software's communication duration and C++ fftw [34] library's computation duration as a reference, which results in an approximately 4 ms delay. Our simulation does not explicitly calculate the noise due to the consecutive RF excitation. However, we use the experimentally measured position noise of MS-SET in dynamic cases reported by [4], in order to capture the effect of the measurement noise on control performance.

In the simulations, the duration of the MS-SET-based tracking pulses t_t shown with the green gradients in Fig. 2 is set to 16.5 ms and average gradient for tracking pulses, which is the average of dephasing, readout and rephasing gradients, in each direction are set to 0.453 mT/m based on data reported by Felfoul et al. [6]. The duration of intra-operational imaging t_i and gradient actuation t_a are kept variable in order to investigate their effect on control performance. While t_a should be always greater than zero, we let t_i to be zero, which indicates no intra-operational imaging, to be a reference for comparison.

A. Actuation Duration

Due to the limitations of the MRI sequence duration on sampling and actuation frequency, tracking and actuation sequences have a maximum closed-loop rate capacity. To quantify the effect of the closed-loop rates on control and estimation performance, we carry out 40 trajectories following simulations for various $\mathscr{N}$ value between 1 to 10. We used 3D sinusoidal trajectories with a 10 s period, and the amplitudes of each axis are independently drawn from [0, 5] mm interval using a uniform distribution, which guarantees the velocities to stay within laminar flow regime. k_d and k_p gains calculated according to (22) and desired damping ratios We calculate the average estimation and trajectory following errors for position and velocity by

$$E_{\mathrm{x,est}} = \frac{1}{N}\sum_{i=0}^{N}\left\|\mathbf{r}_{\mathrm{e,i}}, -\mathbf{r}_{\mathrm{g,i}}\right\|_2, \quad E_{\mathrm{v,est}} = \frac{1}{N}\sum_{i=0}^{N}\left\|\mathbf{v}_{\mathrm{e,i}} - \mathbf{v}_{\mathrm{g,i}}\right\|_2$$

$$E_{\mathrm{x,tra}} = \frac{1}{N}\sum_{i=0}^{N}\left\|\mathbf{r}_{\mathrm{d,i}}, -\mathbf{r}_{\mathrm{g,i}}\right\|_2, \quad E_{\mathrm{v,tra}} = \frac{1}{N}\sum_{i=0}^{N}\left\|\mathbf{v}_{\mathrm{d,i}} - \mathbf{v}_{\mathrm{g,i}}\right\|_2$$

where $\|\cdot\|_2$ is the euclidean distance, N is number of data points, and subscripts g, e and d represents ground truth, estimated and desired trajectory values. We performed simulations with various damping ratios. However, due to the space limitations, we only give the results for $\zeta = 1/\sqrt{2}$. Fig. 3 shows the estimation and trajectory following errors for position and velocity with respect to $\mathscr{N}$ for tracking and actuation sequence with 15 ms actuation. The transparent regions around the data represent the standard deviation of the simulations. The position sensor noise level is shown in the top figure with the red dash line. The data for $\mathscr{N} < 1$ is not given since the controller becomes unstable.

After observing the effect of $\mathscr{N}$, we perform the same trajectory following experiments for varying actuation gradient durations for $\mathscr{N} = 4$ and $\zeta = 1/\sqrt{2}$. In addition to the previous analysis, we also add Gaussian noise on temperature and fluid velocity with the standard deviation of 0.5 °C and 1 mm/s, respectively. The estimation and trajectory following error results are given in Fig. 4 with respect to sequence frequency corresponding to different actuation durations. The transparent regions around the data represent the standard deviation of 40 repetitions of simulation for each frequency. Since the controller becomes unstable, the data corresponded to low frequencies are not presented in the plot.

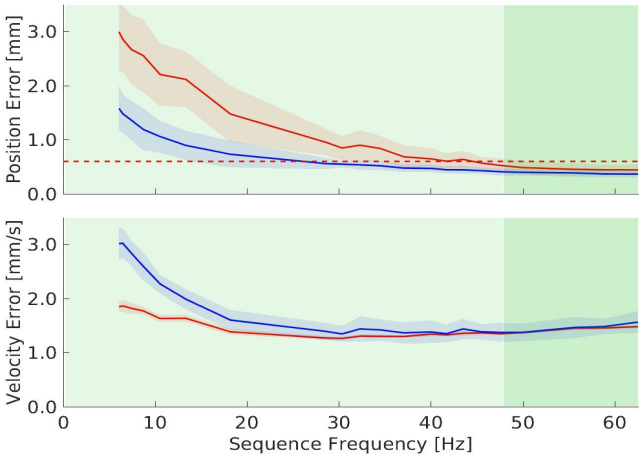

Fig. 4: The simulation plots show average mean-square tracking (red) and estimation (blue) error for the position and velocity with respect to the sequence frequency corresponding to different actuation gradient duration for 40 simulations for each sequence frequency. $\mathscr{N}$ is chosen as $\mathscr{N} = 4$ and damping ratio is chosen as $\zeta = 1/\sqrt{2}$. Horizontal dashed line is the standard deviation of the MS-SET base position sensor. The dark green area represents the cases in which the position data is received in next repetition.

B. Intra-Operational Imaging Duration

Unlike changing actuation durations, changing inter-operational imaging durations also decreases the sequence-averaged actuation gradient, according to (4). Therefore, it should be evaluated separately. In order to evaluate the effect of the intra-operational imaging duration, we performed the same trajectory following experiments 40 times for each intra-operational imaging duration using the sequence scheme shown in Fig. 2 with 15 ms actuation. We simulated gradient pulses of the EPI image shown in Fig. 1.c by approximating it in two parts. The first part is 16 ms long slice selection gradient in the x-direction with 10 mT/m magnitude; the second part is the incremental phase encoding gradient in $-y$ direction with 4.7 µT/m during the rest of the EPI imaging duration. Since the frequency encoding gradients of pulse trains are symmetric, we assume that they cancel each other. We show the estimation and trajectory following accuracy for the position with respect to the number of k-space line contained by the EPI sequence in Fig. 5. Furthermore, we also present example EPI images. The images are matched with the corresponding k-space line numbers in Fig. 5.

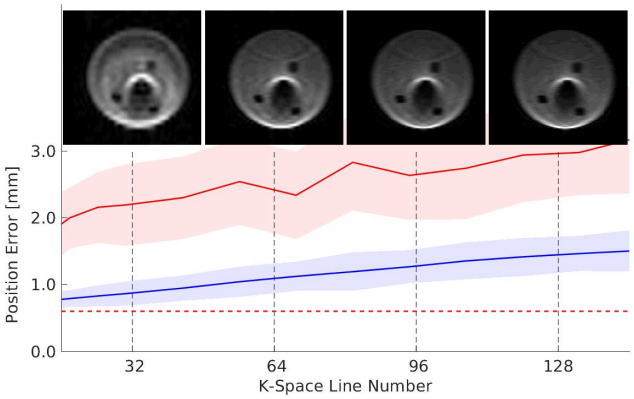

Fig. 5: The simulation plots show average mean tracking (red) and estimation (blue) error of position with respect to different intra-operational image k-space numbers for $\mathscr{N} = 4$ and $\zeta = 1/\sqrt{2}$. The experimental MR images with different resolutions are matched with the k-space line numbers with vertical dash lines.

V. Discussion

By the nature of the MRI-based tracking and actuation, the sampling and control frequencies of the MRI-based robotic platforms are limited to sequence frequency. Fig. 3 clearly shows that the trajectory-following performance of the control scheme depends on the capability of the estimator to observe states of the system accurately. As $\mathscr{N}$ decreases, the velocity estimation accuracy of Kalman filter decreases since the sampling rate becomes insufficient compared to the closed-loop rates. When $\mathscr{N} < 2$, both position and velocity estimation errors increases and result in instability. On the other hand, as $\mathscr{N}$ increases, the system becomes slow enough for Kalman filter to fully capture the dynamics of the system. As foreseen by [24], the estimation accuracy surpasses the accuracy of the position sensor. From Fig. 3, it can be seen that, for $\mathscr{N} > 2$, the position and for $\mathscr{N} > 4$ velocity estimation converge a minimum error level. Therefore, there is no need to further decrease the controller gains to slow down the system. On the contrary, for $\mathscr{N} > 4$, controller gains become so less that despite the good state estimation, the controller fails to track the trajectory. It is also important to note that this drop-out in controller performance depends on the chosen damping ratio.

Fig. 3 already shows that a sequence has a control gain capacity, hence we compared sequences for the same $\mathscr{N}$ and damping ratio, at which the state estimation error converges to its minimum value for both position and velocity. It can be seen from Fig. 4 that, as actuation duration decreases, the position estimation accuracy also increases, and therefore, the trajectory-following accuracy increases. In contrast, for longer actuation duration corresponding to sequence frequency less than 10 Hz, the control scheme cannot handle the random disturbance and becomes oscillatory and eventually unstable for very long actuation durations. Hence, we conclude that higher sequence frequencies are required for robustness in general. Another important point is that the delay in MRI feedback caused by simulated communication and computation times do not drastically worsen the control performance for sequence frequency falling in the dark green region in Fig. 4. On the contrary, due to increasing estimation accuracy, overall control performance improves as the frequency increases.

The introduction of intra-operational imaging to sequence has a similar effect on sequence frequency with actuation duration. When the duration of imaging is increased the estimation and trajectory following accuracy of the system decreases. Results show that the controller can successfully compensate for the effect of imaging sequences in simulations. From Fig. 5, we can estimate the robot position with an average error 2.0 mm for up to 128 k-space lines. Depending on the application this error might be acceptable. However, for higher precision applications, we should consider images with less resolution, such as in Fig. 1a. Furthermore, although it is hard to see from images due to the low resolution in Fig. 1a-d, collecting a higher number of k-space lines for single-shot EPI image creates more prominent warping distortion. The reason for the warping distortion is the accumulation of magnetic inhomogeneity effects throughout the zigzag k-space trajectory. The more k-space lines are collected, the longer the k-space trajectory become, hence the more distortions are observed. The disturbances can be decreased by using multi-shot EPI as in Fig. 1f, or similarly by collecting less k-space lines and reconstructing images using acceleration techniques [12]–[15]. The repetition of EPI images can be further decreased; however, the images become more distorted. In our analysis, we used the shortest imaging duration that gives visually comprehensible images.

In this study, we use a symmetric spherical bead as a robot; therefore, the effect of the rotational motion is ignored. Due to the high main field of MRI, the results could be generalized to any robot geometry with minor modifications in the fluid drag calculation, unless the magnetic core is freely rotating in the robot's shell. Otherwise, the inertial dynamics of the robot including fluid torques should be considered as in [21]. The same controller and estimator could control the translation motion of anisotropic robots with a fixed ferromagnetic core. However, the robot would freely rotate around the MRI's axial direction. On the other hand, an anisotropic body with non-fixed ferromagnetic core requires a more sophisticated controller [21].

The developed control strategy paves the way for intra-operational imaging by demonstrating the possibility of controlling the robot during continuous imaging. When combined with intra-operational imaging, the proposed approach has the potential to eliminate the need for pre-operational position registration and to give the flexibility to move patients during operations. While, the proposed scheme could control the robot in applications like targetted drug delivery, local hyperthermia, and active unclogging, the targetted operation area is limited by the disturbances, such as fluid flow and surface contacts. Our control strategy could navigate the robot in areas like the gastrointestinal tract and urinary system, which are composed of large cavities compared to robot size. However, using the proposed approach in narrower cavities,

such as the spinal fluid and ventricular system, will lead to position error since the state estimator does not include the interaction with the surfaces. For such cases, nonlinear state estimators may be exploited. Furthermore, predictive controllers, which have access to additional information, such as surface contact information obtained from 2D MR image, would mitigate the trajectory-following error. However, the feedback rate of the MRI-based tracking will determine the upper bound of the trajectory-following performance in such applications.

VI. Conclusion

In this paper, an MRI-based magnetic robot control technique with intra-operational imaging is presented using rigid-body simulations which simulates MRI-based gradient actuation and feedback mechanism realistically. The state estimation and controller performance of the overall system is evaluated for various MRI sequence parameters using dynamic robot simulations, which capture important characteristics of MRI-based tracking and actuation. In simulations, we show that due to the limitations in the sampling frequency, the tracking and actuation sequence has an upper limit in terms of the closed-loop system rate. The intra-operational imaging capacity of the presented approach is investigated in terms of number of k-space lines, which can be collected without resulting in significant decrease in the robot control performance. The implementation of the proposed MRI tracking and actuation scheme in real MRI device is a future work. The other future work will be adapting nonlinear state estimators, which could handle more general operating conditions and developing a real-time reconstruction algorithms, which would visualize the anatomy and robot during the actuation.

References

[1] M. Sitti, *Mobile Microrobotics*. MIT Press, Cambridge, MA, 2017.

[2] M. Sitti, H. Ceylan, *et al.*, "Biomedical applications of untethered mobile milli/microrobots." *Proceedings of the IEEE*, vol. 103, no. 2, pp. 205–224, 2015.

[3] O. Erin, M. Boyvat, *et al.*, "Review of magnetic resonance imaging system-driven medical robots," *Advanced Intelligent Systems*, vol. 2, no. 2, p. 1900110, 2020.

[4] O. Felfoul, J.-B. Mathieu, *et al.*, "In vivo MR-tracking based on magnetic signature selective excitation," *IEEE Trans. Med. Imag.*, vol. 27, no. 1, pp. 28–35, 2007.

[5] S. Tamaz, R. Gourdeau, *et al.*, "Real-time MRI-based control of a ferromagnetic core for endovascular navigation," *IEEE Trans. Biomed. Eng.*, vol. 55, no. 7, pp. 1854–1863, 2008.

[6] O. Felfoul, A. T. Becker, *et al.*, "Simultaneous steering and imaging of magnetic particles using MRI toward delivery of therapeutics," *Scientific Reports*, vol. 6, p. 33567, 2016.

[7] C. Dahmen, K. Belharet, *et al.*, "MRI-based dynamic tracking of an untethered ferromagnetic microcapsule navigating in liquid," *International Journal of Optomechatronics*, vol. 10, no. 2, pp. 73–96, 2016.

[8] D. Folio and A. Ferreira, "Two-dimensional robust magnetic resonance navigation of a ferromagnetic microrobot using pareto optimality," *IEEE Trans. Robot.*, vol. 33, no. 3, pp. 583–593, 2017.

[9] R. R. Rzedzian and I. L. Pykett, "Instant images of the human heart using a new, whole-body mr imaging system," *American Journal of Roentgenology*, vol. 149, no. 2, pp. 245–250, 1987.

[10] K. P. Pruessmann, M. Weiger, *et al.*, "Sense: sensitivity encoding for fast MRI," *Magnetic Resonance in Medicine*, vol. 42, no. 5, pp. 952–962, 1999.

[11] M. A. Griswold, P. M. Jakob, *et al.*, "Generalized autocalibrating partially parallel acquisitions (grappa)," *Magnetic Resonance in Medicine*, vol. 47, no. 6, pp. 1202–1210, 2002.

[12] X. Hu and T. Parrish, "Reduction of field of view for dynamic imaging," *Magnetic Resonance in Medicine*, vol. 31, no. 6, pp. 691–694, 1994.

[13] Z.-P. Liang, F. Boada, *et al.*, "Constrained reconstruction methods in mr imaging," *Rev. Magn. Reson. Med*, vol. 4, no. 2, pp. 67–185, 1992.

[14] G. McGibney, M. Smith, *et al.*, "Quantitative evaluation of several partial fourier reconstruction algorithms used in MRI," *Magnetic Resonance in Medicine*, vol. 30, no. 1, pp. 51–59, 1993.

[15] X. Feng, M. Salerno, *et al.*, "Kalman filter techniques for accelerated cartesian dynamic cardiac imaging," *Magnetic Resonance in Medicine*, vol. 69, no. 5, pp. 1346–1356, 2013.

[16] T. Kensicher, J. Leclerc, *et al.*, "Towards MRI-guided and actuated tetherless milli-robots: Preoperative planning and modeling of control," in *IEEE Int. Conf. Intell. Robot. and Syst.* IEEE, 2017, pp. 6440–6447.

[17] L. Arcese, A. Cherry, *et al.*, "High gain observer for backstepping control of a MRI-guided therapeutic microrobot in blood vessels," in *IEEE Int. Conf. on Biomed. Robot. and Biomechatronics*. IEEE, 2010, pp. 349–354.

[18] L. Arcese, M. Fruchard, *et al.*, "Adaptive controller and observer for a magnetic microrobot," *IEEE Trans. Robot.*, vol. 29, no. 4, pp. 1060–1067, 2013.

[19] K. Belharet, D. Folio, *et al.*, "3D MRI-based predictive control of a ferromagnetic microrobot navigating in blood vessels," in *IEEE Int. Conf. on Biomed. Robot. and Biomechatronics*. IEEE, 2010, pp. 808–813.

[20] A. Eqtami, O. Felfoul, *et al.*, "MRI-powered closed-loop control for multiple magnetic capsules," in *IEEE Int. Conf. Intell. Robot. and Syst.* IEEE, 2014, pp. 3536–3542.

[21] O. Erin, H. B. Gilbert, *et al.*, "Elevation and azimuth rotational actuation of an untethered millirobot by MRI gradient coils," *IEEE Trans. Robot.*, vol. 35, no. 6, pp. 1323–1337, Dec 2019.

[22] O. Erin, D. Antonelli, *et al.*, "Towards 5-dof control of an untethered magnetic millirobot via MRI gradient coils," in *IEEE Int. Conf. Robot. and Autom.* IEEE, 2020, pp. 6551–6557.

[23] F. M. White and I. Corfield, *Viscous fluid flow*. McGraw-Hill New York, 2006, vol. 3.

[24] B. Friedland, "Optimum steady-state position and velocity estimation using noisy sampled position data," *IEEE Trans. Aerosp. Electron. Syst.*, no. 6, pp. 906–911, 1973.

[25] P. Vartholomeos, C. Bergeles, *et al.*, "An MRI-powered and controlled actuator technology for tetherless robotic interventions," *Int. J. Robot. Res.*, vol. 32, no. 13, pp. 1536–1552, 2013.

[26] K. Ogata and Y. Yang, *Modern control engineering*. Prentice hall Upper Saddle River, NJ, 2010, vol. 5.

[27] M. Latulippe, O. Felfoul, *et al.*, "Enabling automated magnetic resonance imaging-based targeting assessment during dipole field navigation," *Appl. Phys. Lett.*, vol. 108, no. 6, p. 062403, 2016.

[28] S. Martel, "Microrobotic navigable entities for magnetic resonance targeting," in *Annual International Conference of the IEEE Engineering in Medicine and Biology*. IEEE, 2010, pp. 1942–1945.

[29] W. Lu, K. B. Pauly, *et al.*, "Slice encoding for metal artifact correction with noise reduction," *Magnetic Resonance in Medicine*, vol. 65, no. 5, pp. 1352–1357, 2011.

[30] R. Sutter, R. Hodek, *et al.*, "Total knee arthroplasty MRI featuring slice-encoding for metal artifact correction: reduction of artifacts for stir and proton density–weighted sequences," *American Journal of Roentgenology*, vol. 201, no. 6, pp. 1315–1324, 2013.

[31] N. Koenig and A. Howard, "Design and use paradigms for gazebo, an open-source multi-robot simulator," in *IEEE Int. Conf. Intell. Robot. and Syst.* IEEE, 2004, pp. 2149–2154.

[32] F. E. Jones and G. L. Harris, "Its-90 density of water formulation for volumetric standards calibration," *Journal of Research of the National Institute of Standards and Technology*, vol. 97, no. 3, pp. 335–340, 1992.

[33] J. Kestin, M. Sokolov, *et al.*, "Viscosity of liquid water in the range- 8 c to 150 c," *Journal of Physical and Chemical Reference Data*, vol. 7, no. 3, pp. 941–948, 1978.

[34] M. Frigo and S. G. Johnson, "The design and implementation of FFTW3," *Proceedings of the IEEE*, vol. 93, no. 2, pp. 216–231, 2005.